

**GPPS-TC-2022-0068**

**COUPLED EULERIAN THIN FILM MODEL AND LAGRANGIAN DISCRETE  
PHASE MODEL TO PREDICT FILM THICKNESS INSIDE AN AERO-ENGINE  
BEARING CHAMBER**

**Sandeep Mouvanal**  
**University of Nottingham**  
sandeep.mouvanal@nottingham.ac.uk  
Nottingham, UK

**Kuldeep Singh**  
**University of Nottingham**  
kuldeep.singh@nottingham.ac.uk  
Nottingham, UK

**Richard Jefferson-Loveday**  
**University of Nottingham**  
richard.jefferson-loveday@nottingham.ac.uk  
Nottingham, UK

**Stephen Ambrose**  
**University of Nottingham**  
stephen.ambrose3@nottingham.ac.uk  
Nottingham, UK

**Carol Eastwick**  
**University of Nottingham**  
carol.eastwick@nottingham.ac.uk  
Nottingham, UK

**Kathy Johnson**  
**University of Nottingham**  
kathy.johnson@nottingham.ac.uk  
Nottingham, UK

**Adrian Jacobs**  
**Rolls-Royce plc**  
adrian.jacobs@rolls-royce.com  
Derby, UK

**ABSTRACT**

The interaction of the oil with air produces a highly complex two-phase flow environment inside aero-engine bearing chambers. It is not currently feasible in the design environment to fully resolve all flow physics including thin films and droplets using numerical methods such as volume-of-fluid (VOF) as they are too computationally expensive. Resolving droplets or the film thickness of micron size using computational grids is not practical for large and complex geometries like bearing chambers. Hence, in the present study the Lagrangian discrete phase model (DPM) is used to simulate oil droplets to reduce the computational cost. The DPM model is coupled with the Eulerian thin-film model (ETFM) to predict the film thickness on the chamber walls. In the present study, the capabilities of the thin-film model to predict film thickness throughout the periphery of the chamber are evaluated on the test case of rimming flows for smooth, shock, and pool regimes. Thereafter, a coupled DPM with ETFM model is used to predict the film thickness on a simplified bearing chamber for shaft speeds ranging from 5000 rpm to 15,000 rpm. The predicted film thicknesses on the chamber wall at different shaft speeds are compared and validated with experimental measurements. A sensitivity study on the DPM inlet conditions including oil droplet size and droplet velocity is investigated and presented in the paper and it shows that the knowledge of inlet conditions are vital for predicting the film formation. The effects of additional terms in the enhanced Eulerian thin film model are also investigated here and it is shown that their inclusion helps to capture more physics of the thin film flows.

## 1. INTRODUCTION

Bearing chambers are an annular region surrounding the shaft bearings of aero-engines that contain oil released from the bearing and channel it through scavenge ports to subsequent oil systems. Bearing chambers are subjected to higher temperatures as modern engines are designed to operate at higher shaft speeds and pressure ratios. Aviation lubrication oil has good heat capacity to ensure the effective cooling of engine parts. But they also have a maximum limit of operation temperature above which there is a risk of thermal and oxidation instability which can lead to coking. The maximum operating temperature of jet oil is limited to 204 °C (Exxonmobil, 2021). Thermal management becomes critical in such situations and adequate supply of oil is required to avoid oil fire and coking (Willenborg et al., 2002). This demands a good understanding of the fluid dynamics and oil distribution inside the bearing chamber for better design and development. However, the interaction of shed oil droplets coming out of the bearings with pressurized air from the seal along with rotating air due to the shaft motion makes the flow inside the bearing chamber highly complicated and two-phase in nature as shown in Fig. 1.

Extensive research has been performed both experimentally and computationally for better insight into bearing chamber flows. The first study in this regard was by Wittig et al. (1994) inside a generic bearing chamber. They studied the oil film distribution on the chamber wall and its connection with the shaft speed. Glahn and Wittig (1996, 1999) conducted measurements to investigate the film velocity and its influence on the local wall heat transfer. Gorse et al. (2003, 2006) studied the airflow structure inside the bearing chamber and classified the flow based on the shaft speed and sealing airflow. They classified the flow behaviour as rotation speed-driven mode and sealing air-driven mode. Kurz et al. (2012, 2013); Kurz and Bauer (2014) performed experiments and identified two different flow regimes and their impact on the wall film formation. The first regime occurs at lower shaft speed and is driven by the gravity force, whereas the second regime occurs at relatively high shaft speed where the oil film distribution on the wall becomes more homogeneous. They also studied the effect of various parameters like shaft speed on the scavenging efficiency of the chamber.

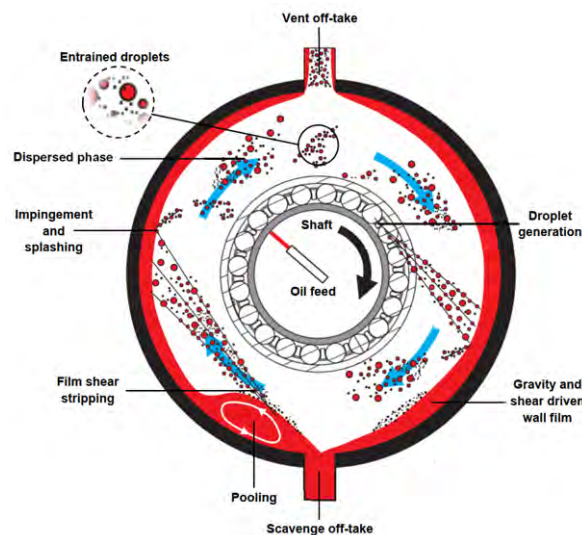


**Figure 1 Two phase complex flow inside bearing chamber (Peduto, 2015)**

An attempt to numerically simulate the complex two-phase flow in the bearing chamber was first performed by Farrall (2000) and Farrall et al. (2001, 2004*b,a*) and was compared with the experimental studies of Wittig et al. (1994). They used ANSYS CFX to solve the flow field along with Lagrangian particle tracking to model the oil droplets. The interaction of droplets and chamber walls was accounted for by a 2D integral model by considering the effect of shear forces and gravity.

The standard approach to studying liquid film flows over walls is by employing the volume of fluid method (VOF). In order to capture liquid film on the bearing chamber surface using the VOF method, the mesh size should be at least one order smaller than the film thickness (Kakimpa et al., 2016*b*), which makes it prohibitively computationally expensive for industrial applications and designs.

In order to reduce the computational cost, currently, research is focusing on coupled approaches. Kakimpa et al. (2016*b*) proposed a coupled (Eulerian thin-film model) ETFM and volume of fluid (VOF) approach to predict film thickness over bearing chamber walls. In the coupled approach, the oil film is resolved by ETFM in the region which is otherwise too expensive to solve by VOF, and in the core flow region is solved by the VOF approach with the limitation of not resolving droplets with the diameters in the order of micrometers. In bearing chambers, the film thickness is around two orders of magnitude smaller compared to the overall dimension of the chamber. In the ETFM approach, the film thickness is not explicitly resolved using the computational grid, instead, the 3D Navier-Stokes equations are depth-averaged across the film thickness to get a set of depth averaged 2D film thickness equations. This helps in reducing the computational cost

considerably. The ETFM approach was used by Ashmore et al. (2003), Kay et al. (2014) and Kakimpa et al. (2016b,a) for predicting rimming flow. This was later extended to the bearing chamber by Wang et al. (2011). Martin et al. (2015) implemented the ETFM model in OpenFOAM CFD code to study a gravity-driven thin wavy fluid films. Meredith et al. (2011); Singh et al. (2019) used the ETFM model to study gravity-driven falling film to predict partial wetting on a flat surface. Singh et al. (2019) studied numerically the film formation in bearing chambers using the ETFM and VOF coupled approach by capturing the wetting and drying behavior on the wall surfaces. The results were found to deviate considerably from experimental measurements but had a close correlation with the previous VOF simulation by Höfler et al. (2015) at a shaft speed of 5000 rpm. Even though ETFM-VOF coupling reduced the computational cost compared to the standard VOF approach the quantitative comparison with experimental results showed that further improvements are required in numerical approaches.

To save computational time and for improved accuracy, Adeniyi et al. (2017); Peng et al. (2019) investigated the coupling of ETFM and DPM models. Recently a coupled discrete phase model (DPM) and ETFM were studied by Nicoli et al. (2019, 2021) for bearing chamber application using OpenFOAM. Droplet generation at the edge of a static insert was modeled through the use of an ETFM edge-separation sub-model and the liquid film was converted to droplets (DPM) based on the edge separation criterion. The focus was to study the droplet size distribution inside the bearing chamber and the film formation very close to the bearing surfaces. But they didn't investigate the film formation and its distribution on the bearing chamber wall which is more challenging to predict and is also an important aspect of thermal management. The film model used in the DPM-ETFM model was having only basic features and not the enhanced features like the capability to model surface force due to surface tension and contact angle.

In this paper, a DPM-ETFM coupled approach with an enhanced ETFM model is used to capture more physics related to film formation and to predict the film thickness distribution in bearing chambers. The main objectives of the current work are to:

- Use the DPM-ETFM coupled approach to predict film formation in the bearing chamber at various operating conditions (shaft speeds).
- Validate the ETFM model to capture smooth, shock, and pooling regimes that are typically observed in bearing chambers.
- Explore the sensitivity of results to inlet conditions like droplet diameter, velocity etc.
- Understand the influence of additional terms like the pressure gradient, spreading, surface tension and contact angle shear in the ETFM model to capture more physics of thin film flow.

## 2. NUMERICAL METHOD

Within the present study, the droplet impingement on the wall surface and the oil film distribution on the bearing chamber wall is of focus. The droplets are modeled using the DPM approach and the thin films are modeled using the ETFM approach. Upon the impingement of droplets on the wall surface, the droplets are absorbed and are converted to wall film. This is achieved by the coupling of the DPM and ETFM models.

In the ETFM model, the three-dimensional Navier-Stokes equations are depth-averaged across the film, resulting in a set of two-dimensional thin-film equations. As such, the ETFM can provide an efficient simulation of segregated wall film flows, for which typically the length scale of the liquid film is significantly smaller than the rest of the domain. When compared to the VOF approach, the ETFM can account for the effects of the thin film without explicitly resolving the very fine grid scales required at the interface.

For the ETFM approach, the depth-averaged continuity equation for a film flow is given by Eqn. 1.

$$\frac{\partial \rho_l h}{\partial t} + \nabla_s \cdot (\rho_l h \vec{V}_l) = \dot{m}_s \quad (1)$$

Where,  $\vec{V}_l$  is the mean film velocity,  $\nabla_s$  is the surface gradient operator,  $h$  the film thickness,  $\rho_l$  the liquid density, and  $\dot{m}_s$  is the mass source per unit wall area, which in the current work accounts for the addition of mass through DPM droplet impingement.

The conservation of film momentum is given by (Eqn.2):

$$\begin{aligned} \frac{\partial \rho_l h \vec{V}_l}{\partial t} + \nabla_s \cdot (\rho_l h \vec{V}_l \vec{V}_l + \vec{D}_V) &= -h \nabla_s P_L + \rho_l h \vec{g}_\tau \\ &+ \frac{3}{2} \vec{\tau}_{fs} - \frac{3\mu_l}{h} \vec{V}_l + \vec{q}_s + \vec{\tau}_{\theta_w} \end{aligned} \quad (2)$$

where the first term on the left-hand side accounts for the transient effects and the second term accounts for inertia effects. In order to improve the stability and to account for the effect of non-uniform velocity distribution across the film thickness,

a correction tensor,  $D_V$ , denoting the differential advection term derived based on the assumption of quadratic film velocity profile is added to the inertia term (Kakimpa et al., 2015, 2016a). The first term on right-hand side is a pressure term and the variable  $P_L$  on the right-hand side of Eqn.2 is defined as (Eqn.3.)

$$\begin{aligned} P_L &= P_{\text{gas}} + P_h + P_\sigma \\ P_h &= -\rho h(\vec{n} \cdot \vec{g}) \\ P_\sigma &= -\sigma \nabla_s \cdot (\nabla_s h) \end{aligned} \quad (3)$$

This accounts for the gas pressure, gravity force normal to the wall (known as spreading), and the surface tension force ( $\sigma$ ) based on the film thickness curvature, respectively. The second term on the right-hand side represents gravity force in the wall tangential direction (parallel to the film). Shear forces on the gas-film  $\tau_{fs}$  and film-wall interfaces are represented by the third and fourth terms on the right-hand side in Eqn. 2. assuming a quadratic film velocity profile. The fifth term is the momentum source term associated with droplet impingement on the film. The last or sixth term  $\vec{\tau}_{\theta_w}$  is the surface force due to film surface tension and contact angle which is critical to model partial wetting and drying processes (Meredith et al., 2011; Singh et al., 2021).

The ETFM is coupled with a Lagrangian Discrete Phase Modelling approach to capture the droplets separated from the bearing and the film formation on the chamber wall. For that the particle trajectories are determined by evaluating Newton's equations for the particulate phase. A one-way ETFM-DPM coupling is used, such that the segregated film can be converted into a dispersed phase, but not the other way. As such, the following equation is solved to obtain the particle trajectories:

$$m_p \frac{du_p}{dt} = F_p \quad (4)$$

where,  $m_p$ , is the mass of the particle. Once the particle force has been calculated, through integrating the particle velocity, the trajectories are determined.  $F_p$  represents the sum of forces acting on the particle. For a standard spherical particle:

$$F_p = F_D + F_g + \vec{F} \quad (5)$$

where  $F_D$  is the dominant drag force and determines the particle trajectory.  $F_g$  is the gravity and buoyancy force and  $\vec{F}$  represents any additional external forces acting on the particle. The viscous drag force,  $F_D$ , provides the force acting on the particle as a result of the difference in velocity between the gas phase and the liquid droplet. For the present study droplets are assumed to be spherical.

### 3. RIMMING FLOW SIMULATION

Highly complex two-phase flow features are observed inside bearing chambers because of the interaction of the lubricant with the air driven by the rotating shaft. Rimming flow is an idealized test case with a representative bearing chamber geometry with two concentric cylinders, one static representing the chamber wall and the other rotating equivalent to the shaft. To simplify further, no inlets or outlets are used. The rimming flow case constitutes an ideal point to start testing the thin film implementation in ANSYS Fluent at various operating conditions. Depending on the shaft speed, Kurz et al. (2012) identified two distinct flow regimes inside the bearing chamber. The first flow regime (regime-1) corresponds to the lower shaft speeds; in this regime, lubricant flow is mainly driven by gravity and dry regions on the bearing chamber wall occurs. The second flow regime (regime-2) appears at higher shaft speeds, here the oil film is observed to be more homogeneous and rotating along the chamber wall due to high shear forces as compared with the first regime.

**Table 1 Description of simulation cases: Rimming flow**

Regime	$h_0$ (mm)	$u_0$ (m/s)	Shear Stress (Pa)
Smooth	0.55	0.512	9.0
Shock	0.7	0.652	9.0
Pool	0.7	0.109	1.5

#### 3.1 Benchmark Test Cases

In the case of rimming flows, three steady flow regimes are identified viz. smooth, shock, and pool, Kakimpa et al. (2015). The schematic of the rimming flow is shown in Fig. 2 (a). A smooth solution is obtained when the surface shear force is sufficient to overcome the gravitational force. This condition is analogous to regime-2 in the bearing chamber reported by Kurz et al. (2012) as shown in Fig. 2 (b). The Pooling flow condition is observed when the gravity force dominates over the shear force, reported as flow regime-1 in experiments of Kurz et al. (2012). A schematic of pooling

flow is shown in Fig. 2 (c). The shock flow condition represents a transition between these two regimes (Fig. 2 (d)). The rimming flow test case is used to assess the ability of the Fluent model to capture three flow regimes described and to assess their performance. The newly enhanced ETFM model implemented in ANSYS Fluent is investigated in the current work. The geometry and boundary conditions for the rimming flow test case are adopted from Kakimpa et al. (2015). The diameter of the cylinder was taken as 222 mm. The test conditions i.e. initial film height, film velocity, and shear stress are given in Table 1. These conditions are specified by a user defined function (UDF).

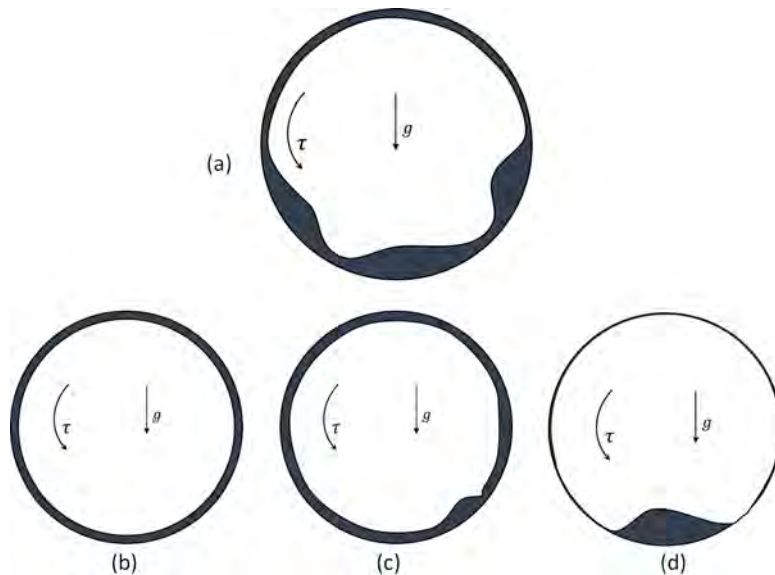


**Figure 2 Schematic of rimming flow (a) general rimming flow case (b) smooth solution (c) Shock solution (d) pool solution**

**Table 2 Coupled model, smoothing level (SL) and smoothing factor (SF) for stability**

Regime	Coupled solver	SL	SF
Smooth	no	no	no
Shock	yes	2	0.5
Pool	yes	2	0.5

The smoothing factor and smoothing level are used for the stability of the solution as shown in Table .1. Smoothing of film surface curvature on a specific face is achieved by blending the film surface curvature values with the neighboring faces in direct or indirect contact. Smoothing of film surface curvature is obtained by an iterative operation. The value of smoothing factor (SF) ranges from 0 to 1 and it determines the magnitude of blending. Smoothing level (SL) is how many levels of the attached neighbouring cells need to be smoothed (Singh et al. (2022)).

### 3.2 Evaluation of ETFM Model Accuracy

#### Smooth Solution

A smooth solution is obtained when the surface shear force is sufficient to overcome the gravitational force and is observed at higher shaft speeds in bearing chambers. An initial film thickness of 0.55 mm on the outer cylinder redistributes to form a circumferential distribution on the wall as shown in Fig. 3 (a). A stable smooth solution is obtained using the ETFM model and the film thickness distribution is comparable with the stable solution obtained by Kakimpa et al. (2015), using a 2D Matlab code as shown in Fig. 3 (a).

#### Shock Solution

Shock flow conditions represent a transition between shear and gravity dominating the film flow. A shock solution is observed to have a smooth global film distribution with a sharp change in the film profile representing the shock region. Kakimpa et al. (2015) obtained a stable shock solution through artificially increasing the surface tension value by one order of magnitude higher than the physical value. Without the change in surface tension value, they observed that the solution was characterized by large oscillations that could lead to numerical errors and loss in mass conservation.

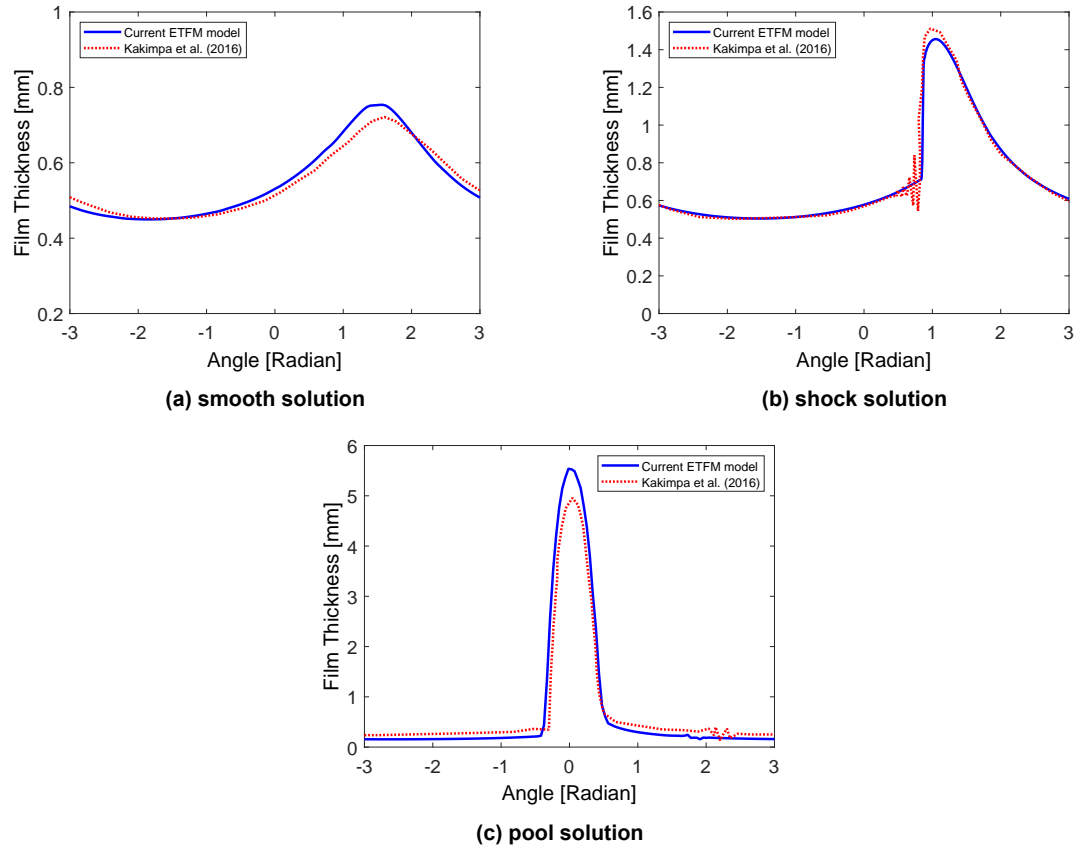


**Figure 3 Film thickness profile for (a) smooth solution (b) shock solution and (c) pool solution and comparison with the 2D Matlab code by Kakimpa et al. (2015)**

In the present work a stable shock solution is able to be obtained in ANSYS Fluent using the ETFM model after the recent enhancements using the coupled solver with smoothing Singh et al. (2021). The values of smoothing level and smoothing factor used for the present simulation are 2.0 and 0.5, respectively as shown in Table .2. The film distribution for the stable shock solution is shown in Fig. 3 (b) and is compared with the stable solution of Kakimpa et al. (2015).

#### *Pool Solution*

When gravitational forces dominate over the shear force, a pool of oil is observed at the bottom of the chamber. This condition is called the pool regime. The angular distribution of film thickness is shown in Fig. 3 (c). As the surface shear is insufficient to overcome gravity and distribute the film evenly throughout the domain, the excess oil in the film pools at the bottom of the domain. A thinner film is drawn out of the pool and circulates around the domain.

As shown in Fig. 3 (a,b and c) the comparison of the present study with Kakimpa et al. (2015) shows good agreement at most of the angular positions, but some variations are observed in the magnitude of film thickness. Such small variations are expected because the result of Kakimpa et al. (2015) was based on a 2D Matlab code and the present study is based on its implementation in ANSYS Fluent with additional features like smoothing of film surface curvature for improved stability of the solution.

#### **4. SIMULATION OF SIMPLIFIED BEARING CHAMBER**

To model the complex two-phase flow inside a bearing chamber, a coupled DPM-ETFM approach is employed here as it can substantially reduce the computational time compared to the VOF approach. A comparison of the simulation result was made with the experimental measurements of Kurz et al. (2012, 2013) and the VOF simulation by Bristot et al. (2016) and Höfler et al. (2015). In the current study, the droplet generation and their distribution in the chamber are modeled using the Lagrangian approach as parcels of particles with a constant diameter. The liquid film is modeled by using the ETFM model. The coupling of DPM and ETFM enables the formation of thin film on the bearing chamber walls based on droplet (particle) impingement and absorption.

The computation domain is shown in Fig. 4a. The corresponding boundary conditions and operating conditions are

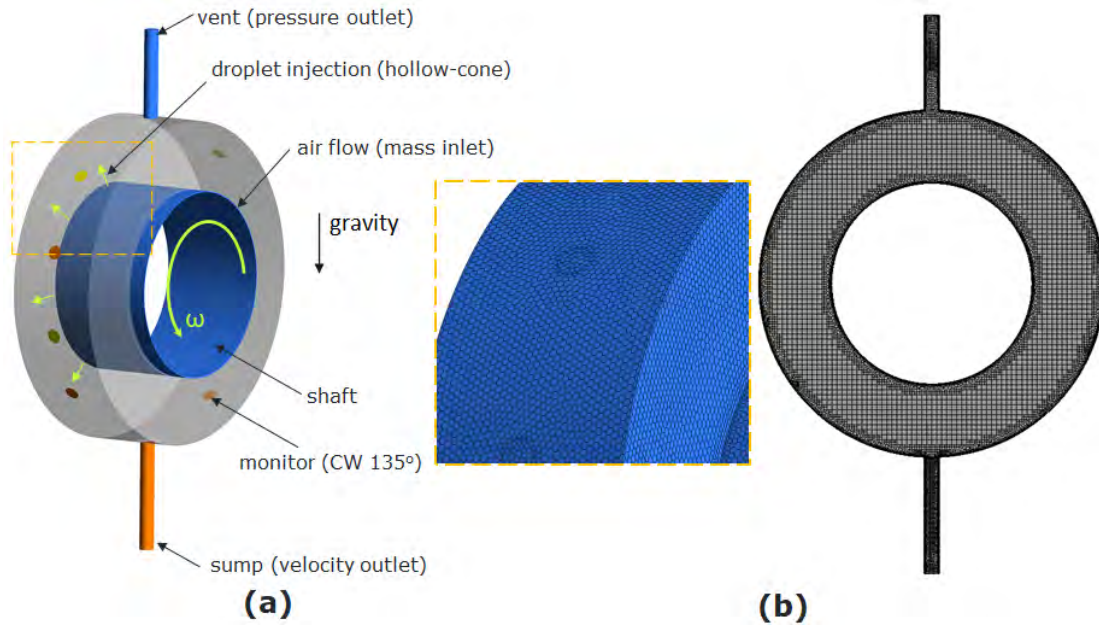


**Figure 4 Simplified bearing chamber based on the dimensions from Kurz et al. (2013). (a) Computational domain and the boundary locations (b) Poly-hex-core mesh, surface and the core region**

**Table 3 Operating conditions and fluid properties**

Operating Conditions		Fluid Properties	
$\dot{m}_{air}$	10 g/s	$\rho_{air}$	2.52 kg/m <sup>3</sup>
$\dot{m}_{oil}$	25.8 g/s	$\mu_{air}$	$2.21 \times 10^{-5}$ kg/ms
$p_{chamber}$	2.7 bar	$\rho_{oil}$	929.5 kg/m <sup>3</sup>
$T_{air}$	373 K	$\mu_{oil}$	$4.83 \times 10^{-3}$ kg/ms
$RPM$	5000, 15000	$\sigma_{oil}$	$2.45 \times 10^{-2}$ N/m
$SR$	4.0		

listed in Table 3. Figure 4b shows the mesh used for the simulation. Here a poly-hex-core mesh is used with a hexahedral mesh in the core region of flow and a uniform polyhedral surface mesh on the wall regions. The overall mesh size is 0.5 million. Droplets are injected as a hollow cone injection with a uniform droplet diameter size of  $100 \mu m$  and the injection velocity magnitude as  $0.5 \times \omega r$ . Here  $\omega$  is the angular velocity of the shaft and  $r$  is the shaft radius. The actual value of droplet diameter is not available from the experiment, as the primary focus by Kurz et al. (2013) was to study the wall film formation on the bearing chamber walls. In reality, the oil droplet size in the bearing chamber will not be a constant value but a distribution with varying sizes based on the shaft speed and the oil shedding mechanism of the bearing. As an engineering assumption, the droplet diameter value is assumed to be  $100 \mu m$  which is of the same order of magnitude assumed in previous studies by Chen et al. (2014) and the droplet velocity is assumed to be 50% of the shaft speed as suggested by Farrall et al. (2004a). Further, a detailed study on the sensitivity of oil droplet size and droplet velocity on wall film formation is also conducted here.

Secondary breakup is ignored in the present study based on the classification of modes of disintegration by Reitz (1978). The classification of the break is given based on Ohnesorge number (Oh) as shown in Eqn. 6 and the Reynolds number as in Eqn.7.

$$Oh = \left( \mu_L / \sqrt{\rho_L \sigma d_o} \right), \quad (6)$$

$$Re_L = (\rho_L U_L d_o / \mu_L), \quad (7)$$

where,  $\mu_L$  is the liquid dynamic viscosity,  $\rho_L$  is the liquid density,  $\sigma$  is the surface tension,  $d_o$  is the length scale (here diameter of the droplet) and  $U_L$  is the relative velocity between the droplet and the core airflow. The values of Oh and  $Re_L$  are plotted and compared with the regimes of atomization for the shaft speeds of 5000 and 15000 rpm with the droplet diameter ranging from  $20 \mu m$  to  $500 \mu m$  as shown in Fig.5. It can be observed that the present cases are in the first and

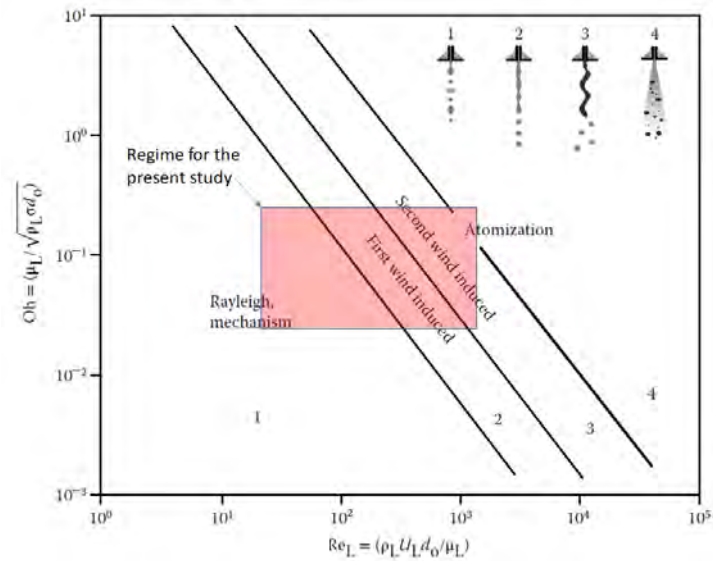


**Figure 5 Classification of liquid break up regime according to Ritz R.D Reitz (1978) and comparison of the present study at 5000 and 15000 rpm**

second wind induced breakup regime and away from the secondary atomization regime. Hence for the simplification of the simulation, secondary breakup is not modelled in the present study.

Since the impact of these DPM input values (diameter and velocity) is not very clear, in the coming sections, a detailed sensitivity study is also presented.

The cases are simulated as the transient problem with a time step size varying from  $1 \times 10^{-4}$  s to  $1 \times 10^{-5}$  s in order to keep the ETFM CFL number below 0.1 for numerical stability. Turbulence was modelled using the  $k - \omega$  SST model by Menter et al. (2003).

In order to estimate the film thickness on the chamber wall, surface monitors are added at various angular positions as shown in Fig. 6. The diameter of these sensors is kept as 1 cm which is equivalent to the sensor diameter in the experimental studies performed by Kurz et al. (2013). The area-averaged values of ETFM film thickness are captured at all these monitor locations for each time steps. To compare the results with the experimental studies, once a quasi steady film thickness profile is obtained, a time averaging procedure is performed for a time equivalent to at least 500 shaft evolutions on each of the sensor locations as shown in Fig. 8.

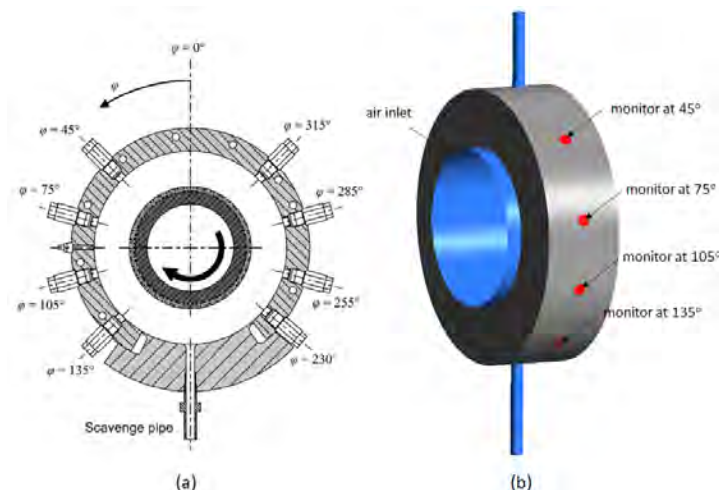


**Figure 6 Angular position of sensors to measure film thickness (a)Location in experiment by Kurz et al. (2013) and (b) the corresponding monitor locations for the CFD study**

#### 4.1 Evaluation of wall film at different shaft speeds

In this section, the oil film formation on the walls of the bearing chamber is studied for two different shaft speeds. One at a high shaft speed value of 15000 rpm and another at a low shaft speed of 5000 rpm. The boundary conditions and operating conditions are as listed in the Table. 3.

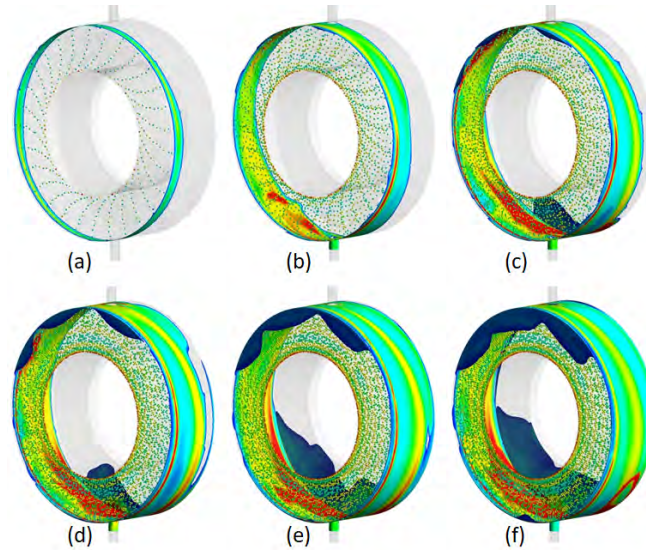


**Figure 7 Oil film formation over time on the surface of chamber wall using ETFM-DPM coupled approach at 15000 rpm: (a) 0.1s, (b) 0.5s, (c) 1.0s, (d) 1.5s, (e) 2.0s and (f) 2.5s**

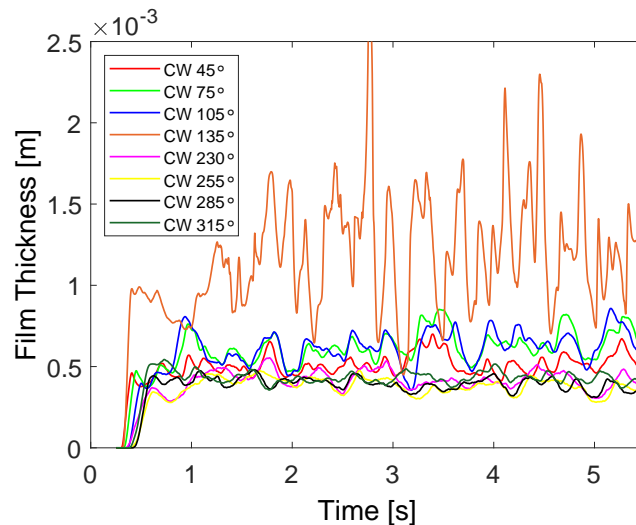


**Figure 8 Temporal variation of film thickness at various monitor locations on the chamber wall at a shaft speed of 15000 rpm**

The droplets which are injected as a hollow cone with the injection velocity as  $0.5 \times \omega r$  hit onto the wall surface and eventually gets absorbed as a thin film. Figure 7 shows the evolution of thin film on the chamber wall surface over time. The film starts forming on the chamber wall near the bearing side and gets spread towards the opposite side. The film is acted upon by the shear force of the core air flow which is rotating due to the shaft speed. At 15000 rpm the shear forces are the dominant force compared to the gravity force acting on the wall films (Kurz et al., 2012). This results in a rotating film on the wall which rotates circumferentially in the direction of rotation of the shaft. Film thicknesses are also monitored at different angular positions and are plotted as shown in Fig. 8. It can be observed that it takes almost 0.5 s for the film to reach sensor locations which are at different angular positions at a mid-axial location. The film thickness fluctuates over time and it can be observed that the sensor marked CW 135° has the highest magnitude and fluctuation. The time-averaged film thickness is obtained by trimming the initial values after reaching a quasi-steady state as shown in Fig. 9 (a). The simulation result shows good comparison with the experimental results Kurz et al. (2013) in terms of the trend and the film thickness magnitude on the chamber wall even though there are some deviations. It can be also observed that the current

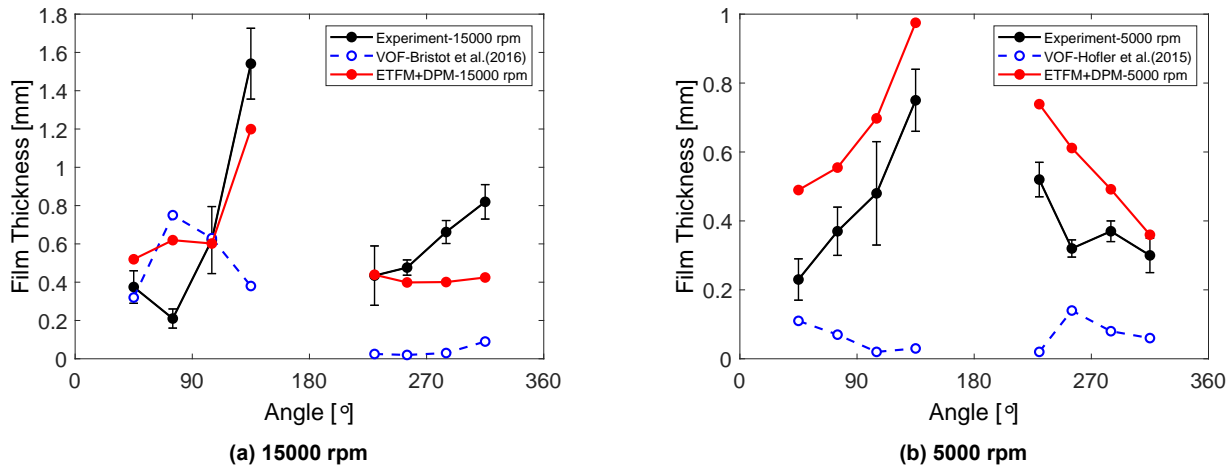


**Figure 9 Comparison of the predicted film thickness at 15000 rpm and 5000 rpm with experiments by Kurz et al. (2013) and VOF numerical study by Bristot et al. (2016); Höfler et al. (2015).**

simulation obtained by ETFM-DPM coupling gives much better agreement than the VOF simulation performed by Bristot et al. (2016). That could be because of the limitation of capturing the dynamics of droplet formation and their transport in the core region of the bearing chamber with a relatively coarse mesh used in the VOF studies. At 15000 rpm, it should be noted that the film thickness distribution on the chamber wall is asymmetric with larger film thickness on the left side of the chamber (CW 45° to CW 135°) compared to a relatively thin film on the right side of the chamber (CW 230° to CW 315°).

For a lower shaft speed of 5000 rpm, the time-averaged film thickness on each monitor points in the angular position is plotted as shown in Fig. 9 (b). At lower shaft speed, the gravity force also becomes a predominant force acting on the wall film along with the shear force. This can be clearly understood by observing the film thickness distribution on the chamber wall. Here at lower shaft speed, the film thickness increases symmetrically towards the bottom of the chamber (at an angle of 180°). This is in good agreement with the experimental measurements of Kurz et al. (2013). The film thickness using the current ETFM-DPM coupling slightly over predicts the film thickness especially in the left side of the chamber (CW 45° to CW 135°), but matches the trend of increasing film thickness towards the sump region (at an angle of 180°). It can be also observed that the current model demonstrates improved agreement compared with the expensive VOF based simulation by Höfler et al. (2015) which needed further mesh refinement to capture the wall film.

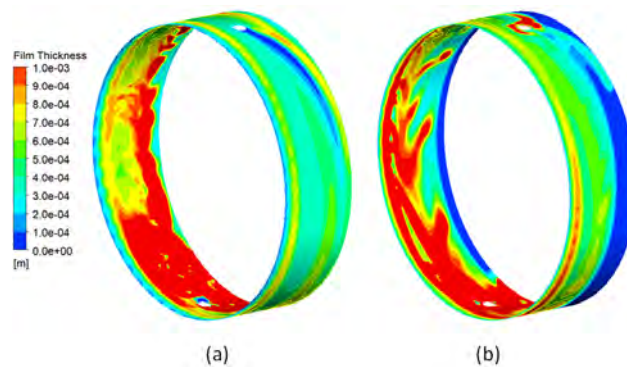


**Figure 10 Film thickness contour on the chamber wall (a) at 15000 rpm (b) at 5000 rpm**

Figure 10 shows the comparison of the film thickness distribution on the chamber wall for shaft speeds of 15000 and 5000 rpm. It can be observed that the film distribution is asymmetric in the 15000 rpm case (Fig. 10 a) with larger film thickness on the left side (CW 45° to CW 135°) of the chamber. This is because at the higher shaft speed the shear force between the oil film and the core airflow becomes dominant which leads to a rotating film in the direction of shaft rotation. This leads to the carry-over of the oil film from the right side (CW 230° to CW 315°) to the left side of the chamber which explains the additional film load on the left side. Whereas in the case with a lower shaft speed of 5000 rpm, gravity becomes the dominant force which leads to a more symmetric film distribution especially towards the sump region.

The strength of the rotating air can be assessed by looking into the momentum flux of the core flow. This can be calculated as shown in Eqn. 8. where,  $\rho_g$  is the gas density and  $u_g$  is the area average circumferential velocity of core flow in the chamber.

$$j_g = \rho_g \bar{u}_g^2 \quad (8)$$

**Table 4 Comparison of momentum flux of the core flow between CFD simulation and Kurz et al. (2013)**

N(rpm)	$\bar{u}_g \left(\frac{m}{s}\right)$ (Kurz et al., 2013)	$\bar{u}_g \left(\frac{m}{s}\right)$	$j_g \left(\frac{kg}{ms^2}\right)$ (Kurz et al., 2013)	$j_g \left(\frac{kg}{ms^2}\right)$
5000	9	8.3	204.3	173.60
15000	27	26.5	1838.7	1769.67

A comparison between Kurz et al. (2013) and the CFD simulations are shown in Table. 4 which shows a close match (within 15% deviation). It should be also observed that there exists a considerable difference in the momentum flux of the core flow at different shaft speeds. Momentum flux is an important parameter that determines the dominance of shear force acting on the film and ultimately influencing the wall film formation on the chamber wall.

#### 4.2 Sensitivity of average oil droplet diameter

Whilst using the coupled DPM-ETFM approach, for the DPM model, the droplet size diameter or its distribution is required as an input along with its velocity and injection location to assign the boundary condition. Ideally, the droplet size should be extracted from experimental measurements or high fidelity CFD simulation focusing on the shedding of oil from bearings to provide accurate injection conditions. This value is often difficult to measure from the experiments and it involves advanced imaging techniques and image analysis tools. In the experimental study of Kurz et al. (2012, 2013); Kurz and Bauer (2014) the main focus was on the film thickness measurement on the wall and droplet size and droplet velocities were not investigated. An alternative is to use a mean diameter such as the Sauter mean diameter from empirical correlations based on rotating disc or rotating cup experiments such Frost (1981), Ahmed and Youssef (2012) or Walton and Prewett (1949). These values vary considerably from one correlation to another, so using different droplet diameters as the input could lead to inaccurate results. Also, there is a lack of understanding of the sensitivity of droplet size and the droplet size distribution on film formation mechanisms.

To study the sensitivity of droplet size on the simulation results, different droplet sizes are investigated ranging from 20  $\mu m$  to 500  $\mu m$  for a fixed oil flow rate and shaft speed (15000 rpm). Film thickness profiles on the chamber wall for all these cases are then compared with the experimental wall film thickness distributions of Kurz et al. (2013).

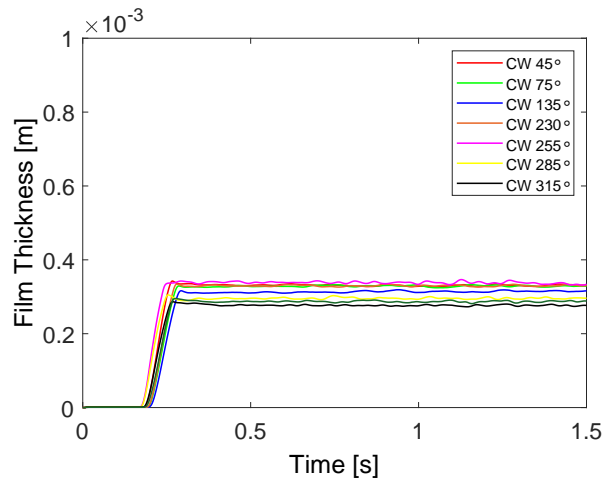


**Figure 11 Temporal evolution of film thickness at various monitor locations on the chamber wall at a shaft speed of 15000 rpm and inlet droplet size of 20  $\mu m$**

Figure 11 shows the temporal variation of the film thickness at all monitors placed at different angular positions in the case of oil droplets with a diameter of 20  $\mu m$ . The magnitude of film thickness and the fluctuation over time are minimal compared with the case of 100  $\mu m$  droplet diameter as in Fig. 8. This can be explained based on the momentum of the particles (droplets). Since these droplets are of smaller size, lesser mass, they are easily carried away by the core flow (circumferentially). This results in lower velocity for the droplets when they reach radially towards the chamber wall as shown in Fig. 12. Droplets with 20  $\mu m$  reach the outer chamber wall with very low velocity (less than 5 m/s) and also their trajectory deviates from that of the 100  $\mu m$  droplets. This implies a smaller mass and momentum is transferred to the wall from DPM to ETFM film in the case of droplets with smaller size which leads to a thinner film on the chamber wall.

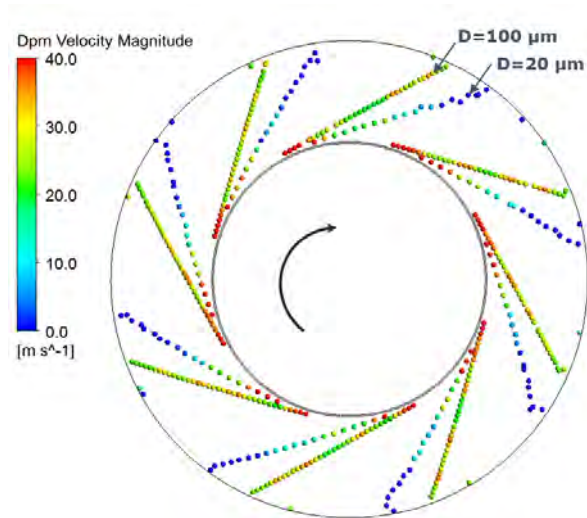


Figure 12 Particle velocity of droplets along its trajectory with the droplet diameter of  $100\mu m$  and  $20\mu m$

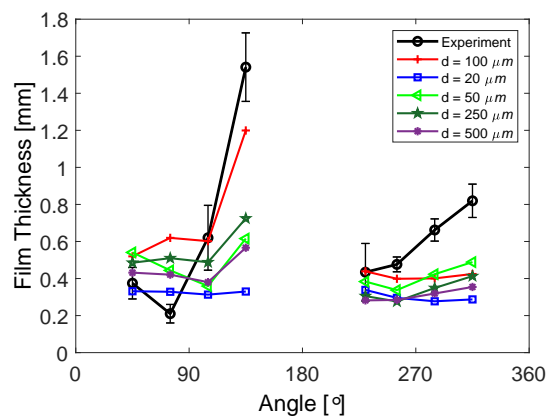
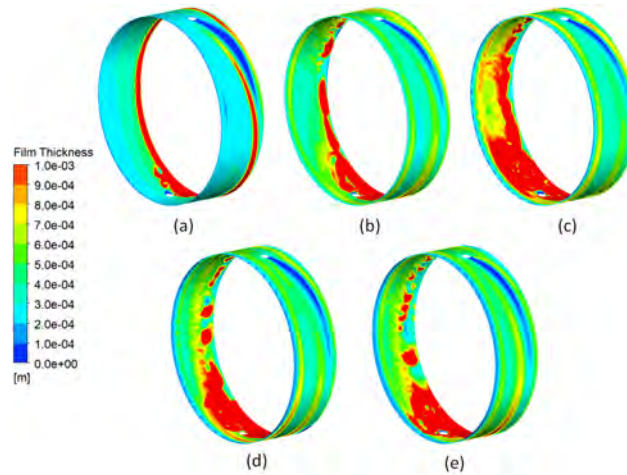


Figure 13 Average film thickness on chamber wall: Comparison at different droplet diameter with experimental study at 15000 rpm

Figure .13 shows the time-averaged film thickness profiles with angular positions for different droplet diameters. In Fig. 14 the film thickness distribution on the chamber wall is plotted for different inlet droplet diameters. It can be observed that there is a considerable difference in the prediction of wall film thickness when varying the injected droplet diameter. This can be attributed to the change in the mass absorbed to the wall film and the momentum exchange between DPM and ETFM for each case. As can be seen the DPM inlet droplet size has a major influence on the film formation mechanism and it is clear that it should be considered carefully when performing aero-engine bearing chamber simulations. The film distribution can significantly vary by choosing a wrong oil droplet size for DPM injection. Hence it is important to obtain the actual droplet size distribution from experiments for applying the inlet boundary condition by choosing different droplet sizes for DPM injection.

#### 4.3 Sensitivity of circumferential velocity of inlet oil droplet on film formation

Here, a sensitivity study is conducted to understand the influence of the magnitude of the circumferential velocity component of DPM inlet droplets. For this study, three different circumferential velocities were used, namely: 10 % of shaft speed; 50 % of shaft speed, and finally 70% of shaft speed. For each of these case studies, the operating conditions such as oil flow rate, scavenge ratio, airflow rate, droplet diameter, and shaft speed are kept constant. The shaft is modelled as rotating at 15000 rpm, and the droplet diameter chosen is  $100\mu m$ . With the droplet circumferential velocity specified as 10 % of the shaft speed, the velocity and momentum of these inlets droplets were not large enough to travel and impinge on the outer chamber wall and were mainly carried away by the core air flow. Under this condition the film formation observed was minimal and did not cover the chamber wall. Between the circumferential velocities of 50 % and 70 % of the shaft speed, a visible difference in the film thickness pattern was observed, as shown in Fig. 15. This influence can be explained based on the mechanism of the discrete particles (droplets) being absorbed on the wall surface as a thin film.



**Figure 14** Film thickness distribution on the chamber wall for different droplet diameter cases (a)  $d= 20 \mu m$  (b)  $d= 50 \mu m$  (c)  $d= 100 \mu m$  (d)  $d= 250 \mu m$  (e)  $d= 500 \mu m$

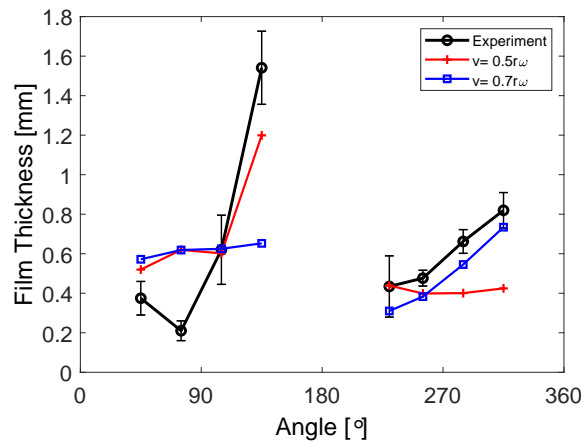


**Figure 15** Average film thickness distribution on the chamber wall at different droplet circumferential velocities

Overall, it can be concluded that the magnitude of the droplet circumferential velocity is an important parameter and influential to the film formation and its thickness. Therefore careful consideration is needed while choosing the value of the circumferential velocity of droplets when specifying DPM injection inlet boundary conditions. Experiments should be conducted to capture droplet velocities but such experiments are often very challenging and need high speed imaging and processing techniques. Clear visualization can be also very challenging due to the splashing of oil from all directions on to the chamber walls. An alternate method is high fidelity CFD simulation using VOF which can resolve the droplets, but they can be very computationally expensive. Another possibility is to perform focused ETFM-DPM coupling simulations close to the bearing outlet as demonstrated by (Nicoli et al., 2019, 2021). The droplet size distribution and droplet velocity from such simulations can be fed as an input into subsequent bearing chamber simulations using the DPM-ETFM coupled.

#### 4.4 Influence of various terms in the enhanced ETFM model on film formation

**Table 5** Description of simulation cases: different terms in the ETFM model

Cases	Description	Terms from Eqn.2
Case a	gravity + surface shear	2, 3 & 4
Case b	case a + pressure grad	1, 2, 3 & 4
Case c	case b + spreading	1, 2, 3 & 4
Case d	case c + surface tension+contact angle shear	1, 2, 3, 4 & 6

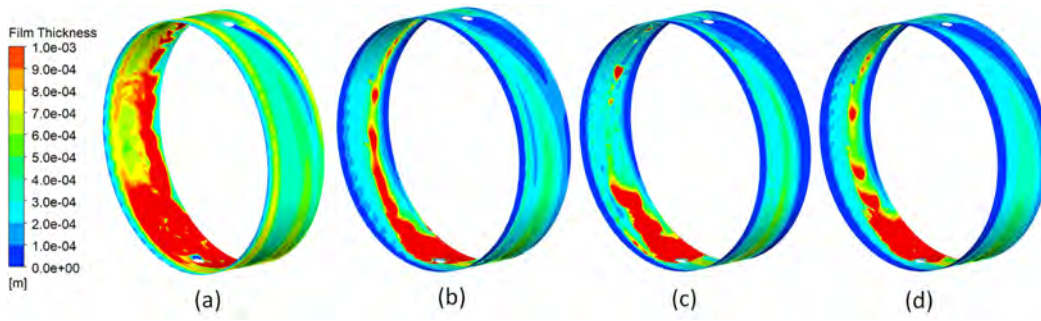


**Figure 16** Film thickness contour on the chamber wall with different terms as listed in Table.5 (a) Case a (b) Case b (c) Case c (d) Case d

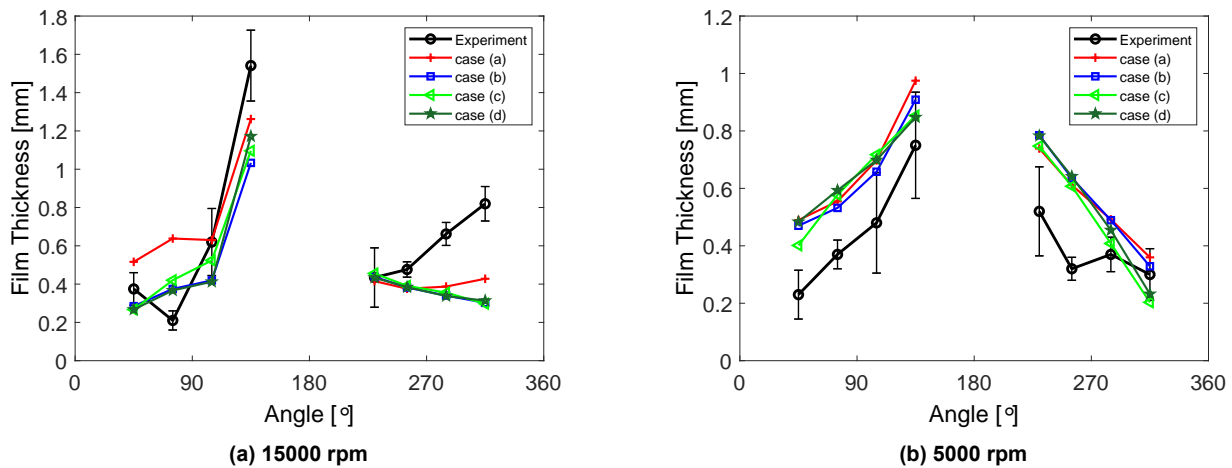


**Figure 17** Average film thickness with different terms as listed in Table.5 for 15000 and 5000 rpm and comparison with experimental measurements of Kurz et al. (2013)

The governing equations of the ETFM model are described in Section 2. The depth-averaged continuity equation is given by Eqn.1 and the conservation of film momentum is given by Eqn.2. There are six terms on the RHS of the film momentum equation. Each of those terms enables the inclusion of more film physics like pressure surface tension, pressure gradient surface shear and spreading.

In this section, the difference between a basic ETFM model (Case a in Table .5, considering only gravity and surface shear) and further enhancement by adding different terms are analyzed. Table .5 shows different cases along with the forces or the terms considered in the film momentum Eqn.2. The case considered is with a shaft speed of 15000 rpm with DPM inlet conditions of  $100 \mu\text{m}$  diameter droplets and a circumferential velocity of  $0.5 \times \omega r$ .

Figure 16 shows the instantaneous film thickness distribution on the chamber wall with different terms enabled in the film momentum equation as described in Table.5. Figure 17 shows time averaged film thickness on the chamber wall at different angular positions. It can be observed that case (a) (Fig. 16a) which is the basic ETFM model consisting of only the gravity and surface shear predicts the wall film without capturing detailed waves on the wall. The basic ETFM model is very simple and numerically stable compared to the other cases with the inclusion of additional terms. With the addition of pressure gradient term, a visible variation in the film distribution of the chamber surface is observed as shown in Fig. 16 b. The addition of pressure gradient term captures the effects of gas-flow pressure and surface tension. Further addition of the spreading term to the pressure gradient component in the film momentum equation enhances the model to capture spreading which is shown in Fig.16 c. And the final term is the surface tension and contact angle effect which helps to capture the wetting and drying phenomenon. In this case at very high rpm the flow is shear driven and hence the effect of wetting and drying is not visible. The time averaged film thickness on the chamber wall does not deviate significantly between all these different cases, which can be clearly observed for 15000 rpm as shown in Fig. 17 (a) and for 5000 rpm as in Fig. 17 (b). These enhancements and additional physics but require ETFM CFL number an order of magnitude lower than the basic model to achieve stable solutions.

## 5. CONCLUSION

In the present work, an approach to simulate the wall film formation in an aero-engine bearing chamber by coupling DPM and ETFM is presented. This method can be an alternative to the expensive VOF simulations which demands extremely fine meshes to resolve droplets, ligaments, and wall films to capture the film formation accurately. Before employing the ETFM-DPM coupled approach, the ETFM model implemented in ANSYS Fluent was tested with a benchmark test case (rimming flow) to study the stability and accuracy. The result shows that ETFM model can satisfactorily capture all the three film flow regimes (smooth flow, shock and pool) observed in the bearing chamber. Simulations were then performed on a representative bearing chamber geometry at different shaft speeds to understand its influence on film formation. At higher shaft speeds a rotating film was observed due to the high influence of the shear force acting on the wall film. An asymmetric distribution of the film was observed on the chamber wall with one side (CW 45° to CW 135°) having a larger film thickness. In the case of lower shaft speeds gravity force dominates the film formation and results in a symmetric film profile towards the sump region of the chamber. A sensitivity study was also conducted on the DPM inlet parameters including droplet diameter and droplet velocity. It was observed that the film formation was highly sensitive to droplet diameter and that it can directly influence the mass absorbed by the film and the impingement process. Similarly, film formation was highly sensitive towards droplet velocity at inlet. Therefore inlet conditions are important and should be considered carefully when performing aero-engine bearing chamber simulations. Where possible experimental measurements should be used to inform inlet conditions. Alternately, high fidelity or alternative validated CFD method should be used to model the bearing shedding process to obtain droplet size and velocity distributions. The influence of various terms in the ETFM model was also studied here. It shows that additional terms like pressure gradient and surface tension can help to capture better film physics but the ETFM CFL number should be an order of magnitude lower for stable solutions.

## NOMENCLATURE

### Acronyms

CFD = Computational Fluid Dynamics  
DPM = Discrete phase model  
ETFM = Eulerian thin film model  
SR = Scavenge ratio  
VOF = Volume of Fluid

### Symbols

$g$  = Acceleration due to gravity  
 $h$  = Film height  
 $j$  = Momentum flux  
 $P$  = Pressure  
 $r$  = Radius of shaft  
 $u$  = Film velocity  
 $V$  = Velocity  
 $Oh$  = Ohnesorge number  
 $Re$  = Reynolds number

### Greek Symbols

$\mu$  = Dynamic viscosity  
 $\rho$  = Density  
 $\sigma$  = Surface tension  
 $\omega$  = Angular velocity  
 $\tau$  = Shear stress

### Subscripts

$g$  = gas  
 $l$  = liquid  
 $p$  = particle  
 $0$  = Initial condition

## ACKNOWLEDGMENTS

The research leading to these results has received funding from the Clean Sky 2 Joint Undertaking under the European Union's Horizon 2020 research and innovation programme under grant agreement No 724625. The calculations were performed using the University of Nottingham High Performance Computing Facility and Sulis, which was funded by the EPSRC on grant EP/P020232/1.

## References

- Adeniyi, A. A., Morvan, H. P. and Simmons, K. A. (2017), 'A coupled euler-lagrange cfd modelling of droplets-to-film', *The Aeronautical Journal* **121**(1246), 1897–1918.
- Ahmed, M. and Youssef, M. (2012), 'Characteristics of mean droplet size produced by spinning disk atomizers', *Journal of Fluids Engineering* **134**(7).
- Ashmore, J., Hosoi, A. and Stone, H. (2003), 'The effect of surface tension on rimming flows in a partially filled rotating cylinder', *Journal of Fluid mechanics* **479**, 65–98.
- Bristot, A., Morvan, H. P. and Simmons, K. A. (2016), Evaluation of a volume of fluid cfd methodology for the oil film thickness estimation in an aero-engine bearing chamber, in 'Turbo Expo: Power for Land, Sea, and Air', Vol. 49712, American Society of Mechanical Engineers, p. V02CT39A007.
- Chen, B., Chen, G., Sun, H. and Zhang, Y. (2014), 'Effect of oil droplet deformation on its deposited characteristics in an aeroengine bearing chamber', *Proceedings of the Institution of Mechanical Engineers, Part G: Journal of Aerospace Engineering* **228**(2), 206–218.
- Exxonmobil (2021), *Mobil Jet Oil II Product Data Sheet*, Exxonmobil. See also URL <https://www.exxonmobil.com/>.
- Farrall, M. (2000), Numerical modelling of two-phase flow in a simplified bearing chamber., PhD thesis, University of Nottingham.
- Farrall, M., Hibberd, S. and Simmons, K. (2001), 'Computational modelling of two-phase air/oil flow within an aero-engine bearing chamber', *ROLLS ROYCE PLC-REPORT-PNR*.
- Farrall, M., Simmons, K., Hibberd, S. and Gorse, P. (2004a), A numerical model for oil film flow in an aero-engine bearing chamber and comparison with experimental data, in 'Turbo Expo: Power for Land, Sea, and Air', Vol. 41693, pp. 409–417.
- Farrall, M., Simmons, S., Hibberd, S. and Gorse, P. (2004b), 'Modeling oil droplet/film interaction in an aero-engine bearing chamber and comparison with experimental data', *ASME Paper No. GT2004-53698* **10**.
- Frost, A. (1981), 'Rotary atomization in the ligament formation mode', *Journal of Agricultural Engineering Research* **26**(1), 63–78.
- Glahn, A. and Wittig, S. (1996), 'Two-phase air/oil flow in aero engine bearing chambers: characterization of oil film flows'.
- Glahn, A. and Wittig, S. (1999), 'Two-phase air/oil flow in aero-engine bearing chambers—assessment of an analytical prediction method for the internal wall heat transfer', *International Journal of Rotating Machinery* **5**(3), 155–165.
- Gorse, P., Busam, S. and Dullenkopf, K. (2006), 'Influence of operating condition and geometry on the oil film thickness in aeroengine bearing chambers'.
- Gorse, P., Willenborg, K., Busam, S., Ebner, J., Dullenkopf, K. and Wittig, S. (2003), 3d-lda measurements in an aero-engine bearing chamber, in 'Turbo Expo: Power for Land, Sea, and Air', Vol. 36886, pp. 257–265.
- Höfler, C., Bauer, H.-J., Kurz, W. and Krug, M. B. (2015), 'Evaluation of the volume-of-fluid method for the numerical modeling of an aero engine bearing chamber', *ISABE 2015 (Awatef Hamed, Faculty Work and Research, College of Engineering and Applied Science)*.
- Kakimpa, B., Morvan, H. and Hibberd, S. (2015), Solution strategies for thin film rimming flow modelling, in 'Turbo Expo: Power for Land, Sea, and Air', Vol. 56734, American Society of Mechanical Engineers, p. V05CT15A026.
- Kakimpa, B., Morvan, H. and Hibberd, S. (2016a), 'The depth-averaged numerical simulation of laminar thin-film flows with capillary waves', *Journal of Engineering for Gas Turbines and Power* **138**(11).

- Kakimpa, B., Morvan, H. and Hibberd, S. (2016b), The numerical simulation of multi-scale oil films using coupled vof and eulerian thin-film models, in 'Turbo Expo: Power for Land, Sea, and Air', Vol. 49682, American Society of Mechanical Engineers, p. V001T01A020.
- Kay, E., Hibberd, S. and Power, H. (2014), 'A depth-averaged model for non-isothermal thin-film rimming flow', *International Journal of Heat and Mass Transfer* **70**, 1003–1015.
- Kurz, W. and Bauer, H.-J. (2014), An approach for predicting the flow regime in an aero engine bearing chamber, in 'Turbo Expo: Power for Land, Sea, and Air', Vol. 45738, American Society of Mechanical Engineers, p. V05CT16A037.
- Kurz, W., Dullenkopf, K. and Bauer, H.-J. (2012), Influences on the oil split between the offtakes of an aero-engine bearing chamber, in 'Turbo Expo: Power for Land, Sea, and Air', Vol. 44700, American Society of Mechanical Engineers, pp. 2251–2259.
- Kurz, W., Dullenkopf, K. and Bauer, H.-J. (2013), 'Capacitive film thickness measurements in a ventless aero-engine bearing chamber—influence of operating conditions and offtake design', *Journal of engineering for gas turbines and power* **135**(11).
- Martin, M., Defraeye, T., Derome, D. and Carmeliet, J. (2015), 'A film flow model for analysing gravity-driven, thin wavy fluid films', *International Journal of Multiphase Flow* **73**, 207–216.
- Menter, F. R., Kuntz, M. and Langtry, R. (2003), 'Ten years of industrial experience with the sst turbulence model', *Turbulence, heat and mass transfer* **4**(1), 625–632.
- Meredith, K., Heather, A., De Vries, J. and Xin, Y. (2011), 'A numerical model for partially-wetted flow of thin liquid films', *Computational Methods in Multiphase Flow VI* **70**, 239.
- Nicoli, A., Jefferson-Loveday, R. and Simmons, K. (2019), A new openfoam solver capable of modelling oil jet-breakup and subsequent film formation for bearing chamber applications, in 'Turbo Expo: Power for Land, Sea, and Air', Vol. 58578, American Society of Mechanical Engineers, p. V02CT41A010.
- Nicoli, A., Johnson, K. and Jefferson-Loveday, R. J. (2021), 'Simulation of a simplified aeroengine bearing chamber using a fully coupled two-way eulerian thin film/discrete phase approach part ii: Droplet behaviour in the chamber', *Journal of Engineering for Gas Turbines and Power*.
- Peduto, D. (2015), *Oil Droplet Impact Dynamics in Aero-Engine Bearing Chambers-Correlations derived from Direct Numerical Simulations*, Logos Verlag Berlin GmbH.
- Peng, K., Jie, L. and Yi, L. (2019), 'Modelling and analysis the thin wall film formation with integrated discrete and continuous phase simulation approach'.
- Reitz, R. D. (1978), *Atomization and other breakup regimes of a liquid jet.*, Princeton University.
- Singh, K., Nicoli, A., Jefferson-Loveday, R., Ambrose, S., Paleo, P., Johnson, K., Mouvanal, S., Cao, J. and Jacobs, A. (2022), Predictions of falling wavy films based on the depth averaged thin film model and its application to aeroengine bearing chamber, in 'Turbo Expo: Rotterdam, The Netherlands', American Society of Mechanical Engineers.
- Singh, K., Sharabi, M., Ambrose, S., Eastwick, C., Jefferson-Loveday, R., Cao, J. and Jacobs, A. (2019), Assessment of an enhanced thin film model to capture wetting and drying behavior in an aero-engine bearing chamber, in 'Turbo Expo: Power for Land, Sea, and Air', Vol. 58578, American Society of Mechanical Engineers, p. V02CT41A027.
- Singh, K., Sharabi, M., Jefferson-Loveday, R., Ambrose, S., Eastwick, C., Cao, J. and Jacobs, A. (2021), 'Modeling of partially wetting liquid film using an enhanced thin film model for aero-engine bearing chamber applications', *Journal of Engineering for Gas Turbines and Power* **143**(4).
- Walton, W. and Prewett, W. (1949), 'The production of sprays and mists of uniform drop size by means of spinning disc type sprayers', *Proceedings of the Physical Society. Section B* **62**(6), 341.
- Wang, C., Morvan, H., Hibberd, S. and Cliffe, K. (2011), Thin film modelling for aero-engine bearing chambers, in 'Turbo Expo: Power for Land, Sea, and Air', Vol. 54617, pp. 277–286.
- Willenborg, K., Busam, S., Roßkamp, H. and Wittig, S. (2002), Experimental studies of the boundary conditions leading to oil fire in the bearing chamber and in the secondary air system of aeroengines, in 'Turbo Expo: Power for Land, Sea, and Air', Vol. 36088, pp. 739–747.
- Wittig, S., Glahn, A. and Himmelsbach, J. (1994), 'Influence of high rotational speeds on heat transfer and oil film thickness in aero-engine bearing chambers'.